Lewis Acid Catalysis Confined in Zeolite Cages as a Strategy for Sustainable Heterogeneous Hydration of Epoxides

Weili Dai,[†,‡,⊥] Chuanming Wang,[§,⊥] Bo Tang,[†] Guangjun Wu,[†,‡] Naijia Guan,[†,‡] Zaiku Xie,[*,§] Michael Hunger,[∥] and Landong Li[*,†,‡]

[†]School of Materials Science and Engineering & National Institute for Advanced Materials, Nankai University, Tianjin 300071, People's Republic of China

[‡]Key Laboratory of Advanced Energy Materials Chemistry of Ministry of Education, Collaborative Innovation Center of Chemical Science and Engineering, Nankai University, Tianjin 300071, People's Republic of China

[§]SINOPEC Shanghai Research Institute of Petrochemical Technology, Shanghai 201208, People's Republic of China

[∥]Institute of Chemical Technology, University of Stuttgart, Stuttgart 70550, Germany

S *Supporting Information*

ABSTRACT: We report a heterogeneous catalysis strategy to the sustainable hydration of epoxides by designing robust Lewis acid catalysts confined in zeolite cages as natural shape-selective nanoreactors. In the case of ethylene oxide hydration, Sn-H-SSZ-13 zeolite exhibits remarkable catalytic performance, with an ethylene oxide conversion above 99% and a monoethylene glycol selectivity above 99%, at approaching stoichiometric water/ethylene oxide ratios and near-ambient reaction temperatures. It is revealed by theoretical studies that partially hydroxylated Sn species are the preferred Lewis acid sites for the hydration of ethylene oxide. The concept of Lewis acid catalysis confined in zeolite cages may be applied in the future in the chemical industry to develop energy-saving and environmentally benign processes.

KEYWORDS: *Lewis acid catalysis, Sn-H-SSZ-13, shape-selective, epoxide hydration, partially hydroxylated Sn species*
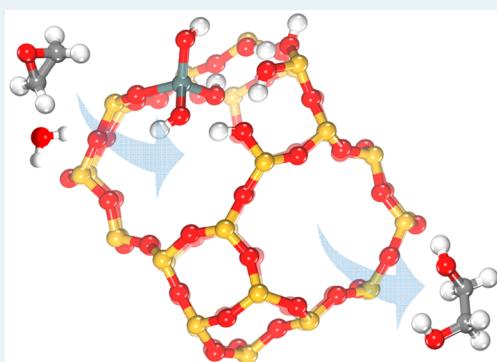
INTRODUCTION

1,2-Diols, e.g. monoethylene glycol (MEG) and 1,2-propylene glycol (PG), are essential ingredients for the production of polyester fibers and resins, engine coolants, antifreeze, etc.[1] MEG is one of the most important diols, and its global demand could be above 28 million tons per year by 2015.[2] Currently, the industrial production of MEG, similar to that of other diols, predominantly involves the liquid-phase thermal hydration of ethylene oxide (EO) at 423−493 K and a large excess of water (H_2O/EO = 20−25) is employed in the actual operation to obtain a high conversion of EO as well as a high selectivity to MEG. In this context, a diluted aqueous MEG solution is produced and huge energy is required for the distillation of the final product from the diluted solution, making EO hydration one of the most energy-intensive processes in the chemical industry with energy consumption of above 6 gJ/ton of MEG.

Catalytic hydration could provide an alternative energy-saving process for the production of MEG from EO. In the past few decades, a variety of acids or bases, e.g. phosphorus-based halides,[3] cation- or anion-exchange resins,[4] supported metal oxides,[5] and amines,[6] have been explored as possible homogeneous or heterogeneous catalysts for the hydration of EO. Despite current achievements, high H_2O/EO ratios are still required, in most cases, to suppress the formation of diethylene

glycol (DEG) and triethylene glycol (TEG), i.e. byproducts from self-condensation of MEG, at high EO conversions. Recently, a key breakthrough has been made by the exploitation of Co^{III}(salen) encapsulated in silica-based nanoreactors as an efficient immobilized homogeneous catalyst for epoxide hydration at approaching stoichiometric H_2O/EO ratios and low reaction temperatures.[7] Immobilized homogeneous catalysts via other strategies, e.g. the cat-in-a-cup concept,[8] might also be applied in EO hydration. However, the stability of the immobilized homogeneous catalyst is a problem and the complex catalyst system as well as complicated preparation procedures might further hinder its industrial application.

In this study, we will demonstrate a heterogeneous catalysis strategy to the sustainable hydration of epoxides: i.e., Lewis acid catalysis confined in zeolite cages. The high selectivity to the desired product is guaranteed by using zeolite cages as natural shape-selective nanoreactors. Meanwhile, a high rate of epoxide hydration is achieved with robust Lewis acid catalysis. In the specific case of EO hydration, an EO conversion above 99% with a MEG selectivity above 99% can be obtained

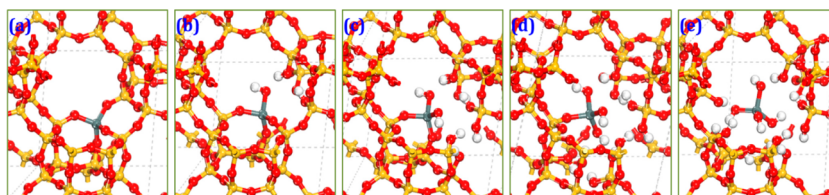**Figure 1.** Closed and open active site structures with partial hydroxylation and full hydroxylation in Sn-H-SSZ-13: (a) closed; (b) $Sn(OSi)_3(OH)$; (c) $Sn(OSi)_2(OH)_2$; (d) $Sn(OSi)(OH)_3$; (e) $Sn(OH)_4$.

simultaneously at approaching stoichiometric H_2O/EO ratios and near-ambient reaction temperatures, making it readily for a large-scale application as an energy-saving and environmentally benign process for MEG production. The concept of Lewis acid catalysis confined in zeolite cages can be extended to other manufacturing processes in chemical industry.

■ EXPERIMENTAL SECTION

Preparation of Zeolite Catalysts. The Na-type zeolite SSZ-13 was provided by Sinopec and converted to its proton form, i.e. H-SSZ-13, by refluxing three times in 0.1 M NH_4NO_3 solutions for 6 h, followed by drying at 343 K for 12 h and calcination at 873 K for 4 h. Zeolite H-SSZ-13 was dealuminated by treatment in 13 M HNO_3 solution at 373 K for 20 h (20 mL/$g_{zeolite}$) and is denoted as deAl-SSZ-13. Sn species were incorporated into the framework of zeolite deAl-SSZ-13 via dry impregnation with $(CH_3)_2SnCl_2$ as the precursor in the glovebox, followed by a calcination at 823 K for 6 h under vacuum. After that, the solid was calcined under flowing air at 823 K for 6 h to derive the product Sn-H-SSZ-13. The obtained zeolite Sn-H-SSZ-13 was further exchanged to a Na-type material with an 0.1 M $NaHCO_3$ solution three times, and the product obtained after calcination is denoted as Sn-Na-SSZ-13. Sn-ZSM-35, Sn-EU-1, and Sn-beta zeolites were prepared via a similar postsynthesis route, and commercial H-ZSM-35 (Si/Al = 14.5), H-EU-1 (Si/Al = 14.7), and H-beta (Si/Al = 13.5) were used as zeolite hosts, respectively.

Characterization Techniques. The specific surface areas of the zeolite samples were determined through N_2 adsorption/ desorption isotherms at 77 K collected on a Quantachrome iQ-MP gas adsorption analyzer. Before the nitrogen adsorption, the samples were dehydrated at 473 K for 2 h. The total surface areas were calculated via the Brunauer–Emmett–Teller (BET) equation, and the microporous pore volumes were determined using the t-plot method. The X-ray diffraction (XRD) patterns of zeolite samples were recorded on a Bruker D8 ADVANCE powder diffractometer using Cu Kα radiation ($\lambda = 0.1542$ nm) at a scanning rate of 4°/min in the region of $2\theta = 5-40°$. The chemical compositions of the samples were determined by inductively coupled plasma emission spectrometry (ICP-AES) on a Thermo IRIS Intrepid II XSP atomic emission spectrometer. Diffuse reflectance ultraviolet–visible (UV–vis) spectra of the zeolite samples were recorded in air against $BaSO_4$ in the region of 200–700 nm on a Varian Cary 300 UV–vis spectrophotometer. Diffuse reflectance infrared Fourier transform (DRIFT) spectra of the samples were measured on a Bruker Tensor 27 spectrometer with 128 scans at a resolution of 2 cm^{-1}. Self-supporting pellets made of sample materials were placed in the reaction chamber and pretreated in flowing dry air at 673 K for 1 h. The spectra were recorded in dry air against KBr as background. Solid-state magic angle spinning nuclear magnetic resonance (MAS NMR) studies were

performed on a Bruker Avance III spectrometer at resonance frequencies of 400.1, 104.3, 79.5, and 149.5 MHz for ^1H, ^{27}Al, ^{29}Si, and ^{119}Sn nuclei, respectively. The ^1H, ^{27}Al, and ^{119}Sn MAS NMR spectra were recorded with a sample spinning rate of 8 kHz, while the ^{29}Si MAS NMR spectra were obtained with a rate of 4 kHz. The ^{27}Al and ^{29}Si MAS NMR measurements were performed with hydrated samples. These samples were exposed to an atmosphere that was saturated with vapor of a $Ca(NO_3)_2$ solution at ambient temperature to be fully hydrated. To avoid damage of the framework, this treatment was done no more than 1 day before the NMR investigations. The samples used for the ^1H MAS NMR studies were dehydrated at 723 K under vacuum (below 10^{-2} Pa) for 12 h. After dehydration, the samples were sealed and kept in glass tubes until they were filled into the MAS NMR rotors in a glovebox purged with dry nitrogen gas. The determination of the number of accessible Brønsted acid sites was performed by adsorption of NH_3 at room temperature. After the NH_3 loading, the samples were evacuated at 453 K for 2 h to eliminate physisorbed ammonia. Quantitative ^1H MAS NMR measurements were performed by comparing the signal intensities of the samples under study with the intensity of an external intensity standard (dehydrated zeolite HNa-Y with a cation exchange degree of 35%). The ^{119}Sn MAS NMR measurements were performed on both hydrated and dehydrated samples. The decomposition and simulation of NMR spectra were carried out using the Bruker software WINFIT.

Catalytic Evaluation. The catalytic hydration of epoxides was performed in a 10 mL autoclave under a nitrogen pressure of 1 MPa. In a typical experiment, the autoclave was charged with a mixture of 10 mmol of EO, 20 mmol of H_2O, and 0.1 g of catalyst, and the reaction was performed with magnetic stirring of 750 rpm at 313 K. After the reaction, the products were qualitatively analyzed by a Shimadzu 2010 GC instrument (Agilent HP-5MS column, 30 m × 0.25 mm × 0.25 μm; FID detector) with octanol as the internal standard. GC peaks were identified by comparison with the retention times of known standard samples and also by means of a Shimadzu GC-MS QP2010 SE instrument equipped with an Agilent HP-5MS column. The reaction conditions, e.g. catalyst/substrate ratio and stirring rate, were optimized to eliminate the diffusion effects. A carbon balance of above 95% was obtained for all experiments. For the plots of the apparent activation energies of the EO hydration, the reaction was performed at different temperatures and a short reaction time was employed to ensure that the EO conversion was below 15% for the calculation of the reaction rate. For the recycling test, the solid catalyst obtained after the reaction was separated by filtration, thoroughly washed with ethanol, and directly reused in the next cycle.

Computation and Modeling. All periodic density functional theory (DFT) calculations were performed using the

Vienna ab initio simulation package (VASP 5.3.5).[9a] The projector augmented wave (PAW) method was employed to describe the electron–ion interactions.[9b] The Bayesian error estimation functional with van de Waals (vdW) correlation (BEEF-vdW) was used.[9c] The plane wave basis set kinetic energy cutoff was set to 400 eV. The sampling of the Brillouin zone was made with the Γ point only. The dimer method was utilized to locate all transition states.[9d] A force threshold of 0.01 eV/Å was used for the structure optimization of all intermediates and transition states. The Sn-H-SSZ-13 system was modeled by a 36T periodic system; the interaction between organic species in different cavities could be completely avoided using this model.[9e,f] The optimized lattice constants (13.72, 13.72, 14.86 Å for CHA framework) were obtained using an 800 eV energy cutoff and a 0.01 eV/Å force threshold. One of the Si atoms was substituted by a Sn atom to produce closed sites; its adjacent Si atoms were then hydroxylated to model open sites and silanol nests. The structures of the investigated closed and open sites are shown in Figure 1.

The harmonic frequency calculations employed a partial Hessian vibrational analysis (PHVA), including the Sn atoms and adjacent OH groups of active sites, water, and organic species parts of involved states. The zero point energies (ZPE), enthalpies, entropies, and Gibbs free energies were then calculated from the harmonic frequencies.

■ RESULTS AND DISCUSSION

Design of Water-Tolerant Lewis Acid Catalysis Confined in Zeolite Cages. For the ring-opening hydration of EO, the reactants EO and H_2O, the target product MEG, and the byproducts DEG and TEG have quite different kinetic diameters and diffusion behaviors. Therefore, it is possible to achieve high MEG selectivity via simple diffusion control. Inspired by the great success of zeolites in molecular shape-selective catalysis,[10] a series of easily available aluminosilicate zeolites with different framework topologies have been examined in the present study. The underlying principle is that the reactants EO and H_2O as well as the target product MEG could easily diffuse through the pore windows of the zeolite, while the byproducts DEG and TEG could not. In this way, the reactants EO and H_2O diffuse into the zeolite cages through pore windows, react within cages, windows with byproducts remaining in the cages due to steric hindrance. By comparison of the diameters of the reactant and product molecules with the pore-limiting diameters of zeolites (calculated from ZEOMICS[11]), we found that zeolites with GIS, CHA, and PHI structures, all characterized by eight-membered rings, are possible candidates for the shape-selective hydration of EO (Figure 2a). SSZ-13, a high-silica zeolite with the chabazite structure,[12] should be the most promising zeolite due to its chabazite cages with a largest diameter of 0.8 nm as natural nanoreactors for the EO hydration as well as its remarkable stability. In addition to the MEG selectivity derived from the diffusion control through the pore windows of zeolite, the use of chabazite cages as nanoreactors also contributes to the MEG selectivity during EO hydration. Since the byproducts DEG and TEG come from the self-condensation of the target product MEG, reaction in the confined space of chabazite cages with H_2O and EO as space fillers can efficiently reduce the collision probability of two or more MEG molecules and, therefore, suppress the formation of byproducts. The schematic illustration of EO hydration to MEG over CHA zeolite is shown in Figure 2b.
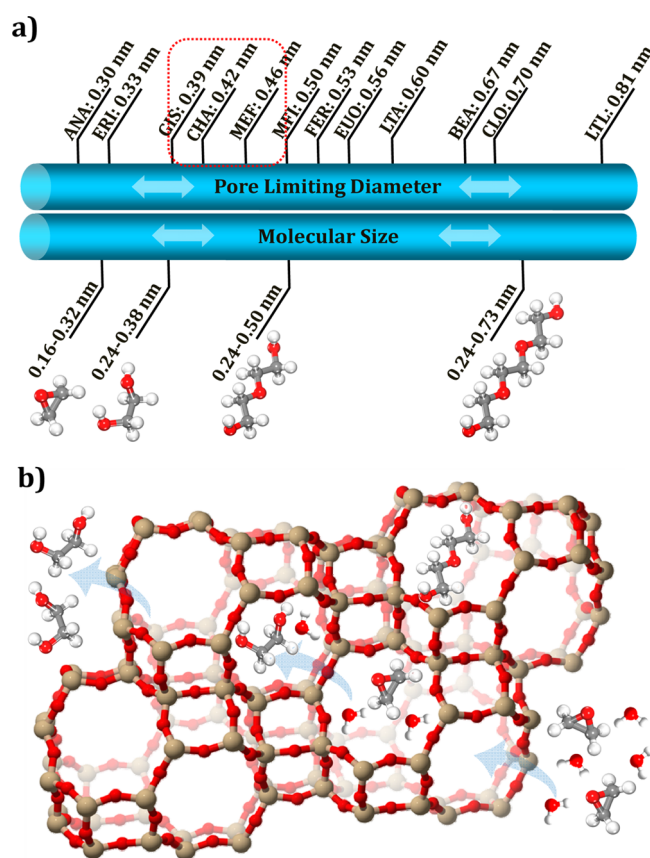

Figure 2. (a) Exploration of the zeolite framework topology for shape-selective catalysis. (b) Schematic illustration of EO hydration to MEG over CHA zeolite.

After the problem of limited product selectivity was solved by using shape-selective catalysts, the catalyst activity became the focus of the present work. Generally, the hydration of epoxides can be catalyzed by Brønsted acids, e.g. anion exchange resins,[4b] or Lewis acids, e.g. metal triflates.[13] Sn-zeolites have been developed as a specific type of strong Lewis acidic catalyst.[14] The most attractive feature of Sn-zeolites is that the Lewis acid sites are tolerant to polar and protic solvents, e.g. water, which makes them essentially different from most conventional Lewis acid catalysts and applicable in several very important reactions in aqueous media, e.g. sugar isomerization and epimerization.[15] Considering that the efficient activation of molecules with C−O bonds has been acknowledged with Sn-zeolites, we propose that Sn-SSZ-13 should be a robust catalyst for EO hydration.

Preparation and Characterization of the Catalyst Systems. The Sn-H-SSZ-13 zeolite was prepared via a two-step postsynthesis strategy, consisting of creating vacant T sites with associated silanol groups by partial dealumination of H-SSZ-13 and subsequent dry impregnation of the resulting deAl-SSZ-13 with organometallic dimethyltin dichloride.[16] It should be noted that the dimethyltin dichloride molecule is relatively large and its diffusion through the small pore windows of SSZ-13 is difficult. In the preparation process, the decomposition of dimethyltin dichloride can proceed by sequential loss of methyl radicals,[17] and $SnCl_2$ with a much smaller kinetic diameter may act as the Sn precursor. The structure changes during the postsynthesis of zeolite catalysts were investigated by XRD, DRIFT, and NMR, as shown in Figure 3. Typical diffraction lines characteristic for the CHA topology are observed for all
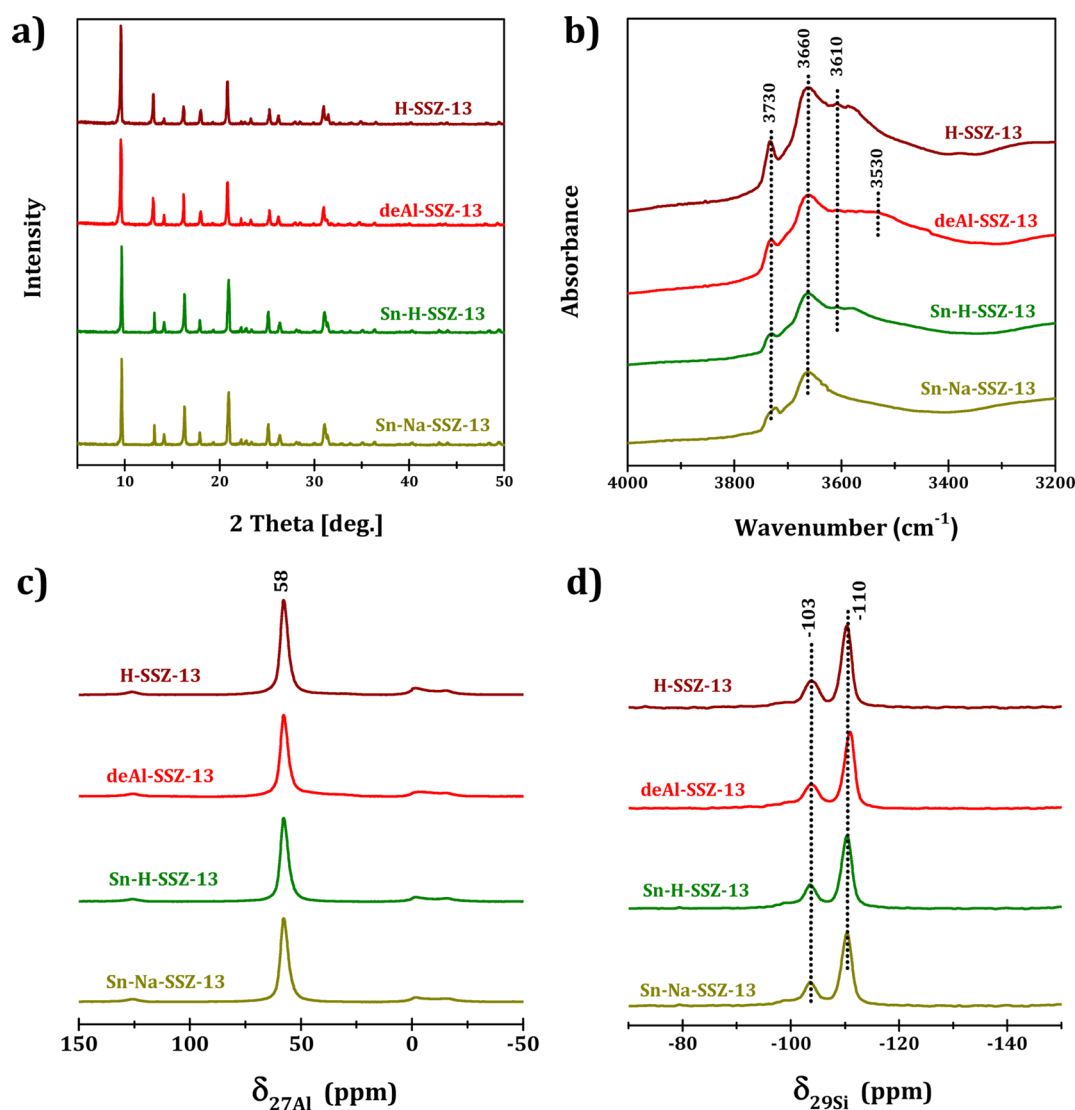
Figure 3. (a) XRD patterns of zeolite samples. (b) DRIFT spectra of zeolite samples. (c, d) ^{27}Al and ^{29}Si MAS NMR spectra of zeolite samples.

Table 1. Physicochemical Properties of the Zeolite Catalysts under Study

sample	n_{Si}/n_{Al}[a]	n_{Sn}[a] (mmol/g)	n_{Si}/n_{Sn}[a]	S_{BET}[b] (m^2/g)	V_{micro}[c] (cm^3/g)	$n_{Si(OH)Al}$[d] (mmol/g)
H-SSZ-13	8.4			823	0.28	1.17
deAl-SSZ-13	9.5			774	0.26	0.97
Sn-H-SSZ-13	9.5	0.17	98	780	0.27	0.94
Sn-Na-SSZ-13	9.5	0.16	98	769	0.26	0

[a]Determined by ICP-AES. [b]Determined by N_2 adsorption. [c]Micropore volume was estimated by using the t-plot method. [d]Determined by ^1H MAS NMR.

zeolite samples, ruling out a collapse of the zeolite framework during the postsynthesis modification process (Figure 3a). The results are consistent with those of the N_2 adsorption/desorption analysis, where no significant loss in surface areas and micropore volumes could be observed (Table 1). The DRIFT spectrum (Figure 3b) of the parent zeolite H-SSZ-13 exhibits several characteristic bands in Figure 3.

Typical diffraction lines characteristic for the CHA topology are observed for all zeolite samples, ruling out a collapse of the zeolite framework during the postsynthesis modification process (Figure 3a). The results are consistent with those of the N_2 adsorption/desorption analysis, where no significant loss in surface areas and micropore volumes could be observed

(Table 1). The DRIFT spectrum (Figure 3b) of the parent zeolite H-SSZ-13 exhibits several characteristic bands in the hydroxyl stretching region: Bands appear at 3730 cm^{-1} due to isolated external Si−OH groups, at 3605 cm^{-1} due to bridging hydroxyls Si−OH−Al, and at 3665 cm^{-1} due to Al−OH groups.[18] The sample treatment in concentrated HNO_3 results in partial dealumination, accompanied by an increase in the n_{Si}/n_{Al} ratio from 8.4 to 9.5 and the appearance of a broad weak IR band centered at 3533 cm^{-1}. This band is due to hydroxyl nests with hydrogen-bonded Si−OH groups located at the vacant T sites in the dealuminated zeolite deAl-SSZ-13.[16b] Dry impregnation of deAl-SSZ-13 with a Sn precursor induced a slight decrease in the intensity of the IR band at 3730 cm^{-1} and
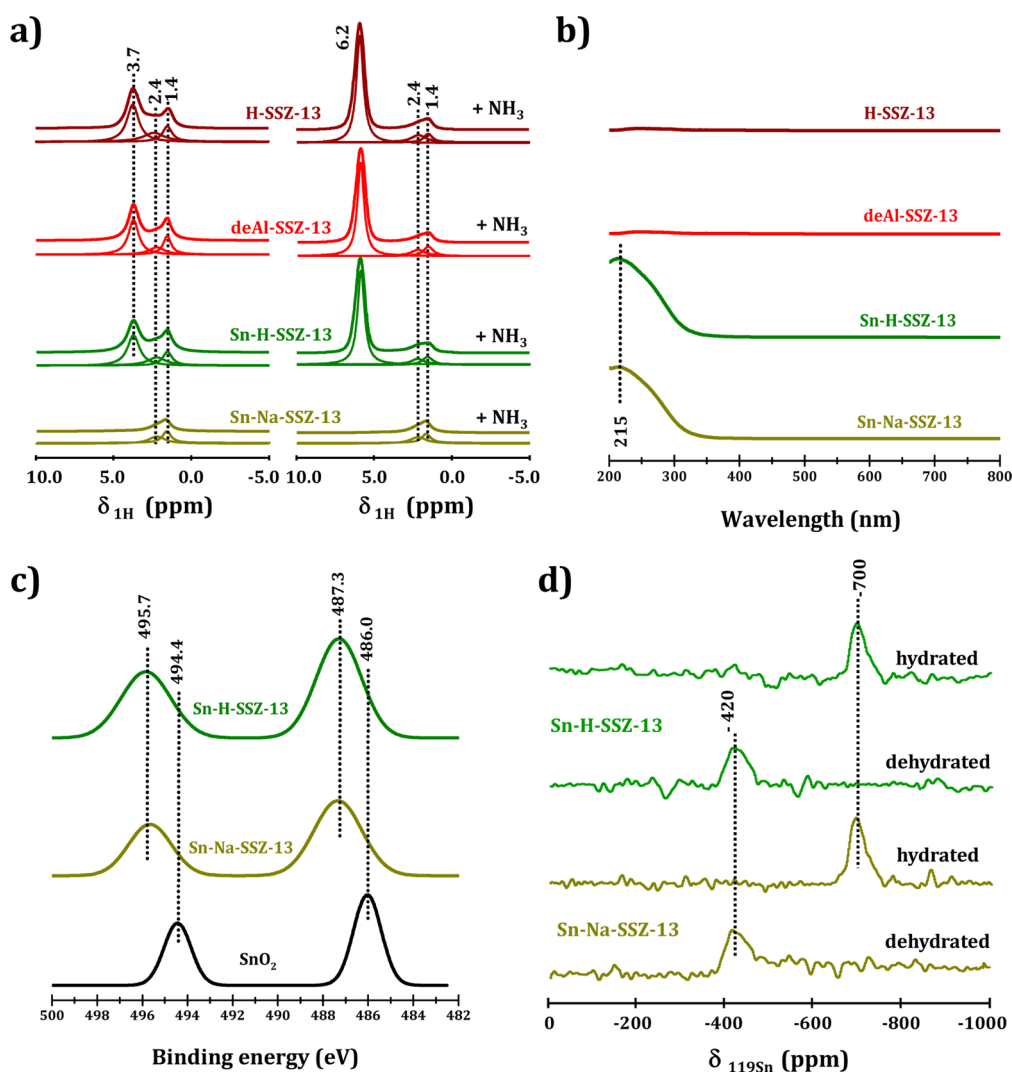
Figure 4. (a) ^{1}H MAS NMR spectra of as-prepared zeolite samples before and after NH_3 loading. (b) UV−vis spectra of as-prepared zeolite samples. (c) Sn 3d XPS of Sn-H-SSZ-13, Sn-Na-SSZ-13, and reference SnO_2 samples. (d) ^{119}Sn MAS NMR of dehydrated and hydrated Sn-H-SSZ-13 and Sn-Na-SSZ-13 samples.

the near-disappearance of the IR band at 3533 cm^{−1}. This finding indicates that Sn species react with the aforementioned silanol groups to incorporate into the CHA zeolite framework. Finally, exchanging the Brønsted acidic bridging hydroxyls in Sn-H-SSZ-13 with Na^{+} results in the disappearance of the IR band at 3605 cm^{−1} for Sn-Na-SSZ-13.

The ^{27}Al MAS NMR spectra of all zeolites under study (Figure 3c) are dominated by strong signals of tetrahedrally coordinated framework Al atoms at ca. 58 ppm and very weak signals of octahedrally coordinated extraframework Al species at ca. −2 ppm,[19] revealing the intact structure of the zeolite samples under study and the high resistance of the CHA structure toward dealumination. The ^{29}Si MAS NMR spectra of all zeolites (Figure 3d) are dominated by strong signals of framework $Si(OSi)_4$ species ca. −110 ppm and weak signals of framework $Si(OSi)_3(OAl)$ species or $Si(OSi)_3(OH)$ at ca. −103 ppm.[20] Furthermore, the changes in the hydroxyl groups in the SSZ-13-based zeolites during postsynthesis modification were further quantitatively analyzed by ^{1}H MAS NMR spectroscopy (Figure 4a). For the parent zeolite H-SSZ-13, a strong signal at 3.7 ppm due to bridging hydroxyl Si(OH)Al groups (NH_3 adsorption leads to the formation of ammonia

ions with signal at 6.2 ppm), a weak signal at 1.4 ppm due to silanol groups at framework defects, and a weak signal at 2.4 ppm assigned to hydroxyl groups bonded to Al species could be observed.[19,21] With partial dealumination, a distinct decrease in the concentration of Brønsted acidic bridging hydroxyls (from 1.17 to 0.97 mmol/g; Table 1) was observed, while no significant changes in Brønsted acidic bridging hydroxyls (0.97 versus 0.94 mmol/g) could be found after Sn incorporation. According to the DRIFT spectra (Figure 3b), the Sn species should be incorporated into the CHA-type framework upon reaction with hydroxyl groups in silanol nests created from the removal of framework Al atoms. The ratio of n_{Sn} replacing the n_{Al} removed during dealumination was calculated to be 0.85, which indicates an approaching stoichiometric replacement of framework Al atoms by Sn atoms during postsynthesis modification. In this case, the location of Sn species in zeolite crystals should be determined, in principle, by the Al atoms removed from the CHA framework. The exchange of zeolite Sn-H-SSZ-13 with Na^{+} cations results in the complete disappearance of the ^{1}H MAS NMR signals caused by Brønsted acidic bridging hydroxyls in Sn-Na-SSZ-13, which is in good agreement with the results obtained by DRIFT spectroscopy.
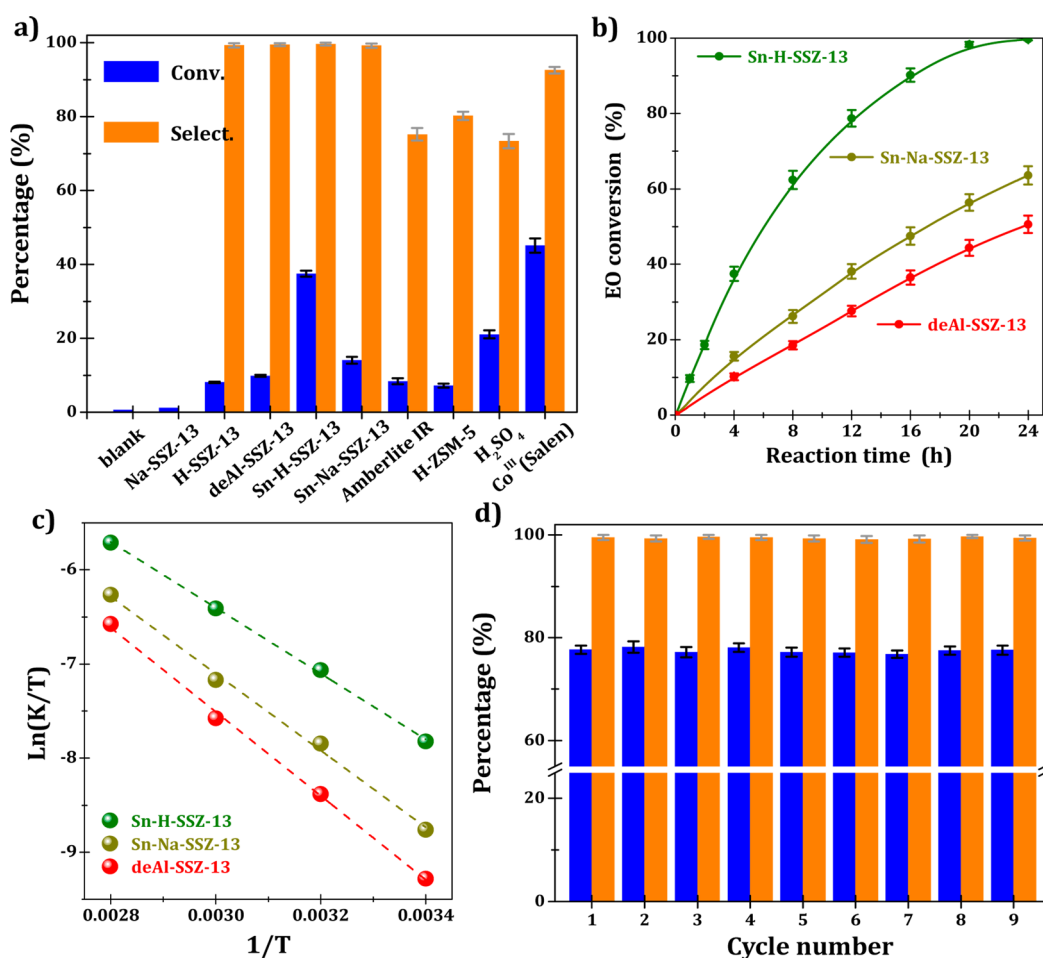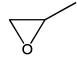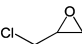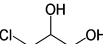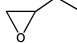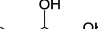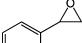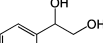
Figure 5. (a) EO conversion and MEG selectivity catalyzed by different catalysts. Reaction conditions: temperature 313 K; $H_2O/EO = 2$; time 4 h. (b) Kinetic plots of EO hydration catalyzed by different zeolite catalysts. Reaction conditions: temperature 313 K; $H_2O/EO = 2$. (c) Kinetic plots of EO hydration with reaction temperature catalyzed by different zeolite catalysts based on the Eyring equation. On Sn-H-SSZ-13, Sn-Na-SSZ-13, and deAl-SSZ-13, the enthalpy barriers are estimated to be 0.30, 0.35, and 0.38 eV, respectively; the entropy contributions to the Gibbs free energy barrier at 313 K are 0.53, 0.50, and 0.49 eV, respectively. (d) Recycling tests of EO hydration catalyzed by Sn-H-SSZ-13. Reaction conditions: temperature 313 K; $H_2O/EO = 2$; time 12 h.

NMR spectroscopy with ^{13}C-2-acetone ($CH_3{}^{13}COCH_3$) adsorption was applied to study the acidic properties of the calcined samples. As shown in Figure S1 in the Supporting Information, a sharp signal at 220 ppm is observed for acetone adsorbed on the Brønsted acid sites of the SSZ-13 samples, whereas the 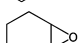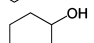very weak shoulder signal at ca. 236 ppm is due to acetone adsorbed on Lewis acid sites.[22] The other signals at 214 and 205 ppm are due to the physisorbed acetone or the products of bimolecular and trimolecular reactions of acetone.[22a,d] In comparison with deAl-SSZ-13, the intensities of the signal at 236 ppm in Sn-H-SSZ-13 and Sn-Na-SSZ-13 dramatically increase, indicating the formation of new Lewis acid sites via the incorporation of Sn species into the CHA zeolite framework. Additionally, the signal due to Brønsted acid sites (220 ppm) disappears in Na-Sn-SSZ-13, in accordance with the FTIR and ^1H MAS NMR results.

To clarify the existence states of Sn species in the CHA-type zeolite framework, UV−vis, XPS, and ^{119}Sn MAS NMR spectroscopic investigations were performed. As shown in the UV−vis spectra in Figure 4b, the dehydrated zeolites Sn-H-SSZ-13 and Sn-Na-SSZ-13 exhibit similar intense absorption bands at ca. 215 nm arising from the ligand-to-metal charge transfer from O^{2-} to Sn^{4+}, which is characteristic of isolated tetrahedrally coordinated Sn atoms in the zeolite framework.[14d,16a] The UV−vis results reveal that framework Sn species are the dominating species in the dehydrated zeolite samples. In the Sn 3d XPS of the dehydrated zeolites Sn-H-SSZ-13 and Sn-Na-SSZ-13 (Figure 4c), two signals at binding energy values of 487.3 and 495.7 eV, caused by $3d_{5/2}$ and $3d_{3/2}$ photoelectrons of tetrahedrally coordinated framework Sn species, can be observed.[23] For comparison, binding energy values of 486.0 and 494.4 eV were observed for the Sn atoms in SnO_2. In the ^{119}Sn MAS NMR spectra of dehydrated Sn-H-SSZ-13 and Sn-Na-SSZ-13 (Figure 4d), signals centered at −420 ppm appeared. According to Davis et al.,[24a] these signals can be ascribed to tetrahedrally coordinated framework Sn species in open arrangements. Minor framework tetrahedral Sn species in a closed arrangement with NMR signals centered at −443 ppm might also exist but overlap with the dominant signals at −420 ppm. After hydration, the NMR signals at −420 ppm disappear and new signals at −700 ppm could be observed instead. The signals at −700 ppm originate from Sn species in a higher coordination state, similar to the case of hydrated Sn-beta zeolites prepared by hydrothermal synthesis.[24] Since dominant tetrahedrally coordinated Sn species in an open arrangement are obtained in dehydrated samples, the Sn species

Table 2. Hydration of Various Epoxides Catalyzed by Sn-H-Zeolite Catalyst[a]

Catalyst	n_{Si}/n_{Al} [b]	n_{Si}/n_{Sn} [b]	T (K)	Time (h)	Substrate	Conv. (%) [c]	Product	Select. (%) [c]
Sn-H-SSZ-13	9.5	98	313	24	ethylene oxide	99.7	HO⌒OH	99.5
			333	8	propylene oxide	72.5	HO⌒⌒OH	98.1
Sn-H-ZSM-35	18.9	72	353	12	Cl-epoxide	38.3	Cl⌒CH(OH)⌒OH	99.5
			313	24	ethylene oxide	98.5	HO⌒OH	77.2
Sn-H-EU-1	23.6	67	313	6	propylene oxide	95.8	CH(OH)⌒OH	95.8
			313	24	ethylene oxide	99.8	HO⌒OH	75.9
			313	1.5	styrene oxide	99.7	Ph-CH(OH)⌒OH	99.9
Sn-Beta	>1800	51	313	6	cyclohexene oxide	90.2	trans-cyclohexane-1,2-diol	92.7
			313	24	ethylene oxide	>99.9	HO⌒OH	70.2

[a]Reaction conditions: 10 mmol of epoxide, 20 mmol of H_2O, 0.1 g of catalyst. [b]Determined by ICP-AES. [c]Determined by GC and GC-MS.

should exist in the form of octahedrally coordinated Sn species, also in an open arrangement after hydration. It should be mentioned that no ^{119}Sn MAS NMR signal at −604 ppm originating from SnO_2 could be observed either for dehydrated or for hydrated zeolite samples, ruling out the formation of oxide-like species. Moreover, exchanging the hydroxyl protons in zeolite Sn-H-SSZ-13 with Na^+ cations (Sn-Na-SSZ-13) does not change the state of the Sn species at all.

On the basis of the aforementioned characterization results, we come to the conclusion that the Sn species were incorporated into the CHA framework of SSZ-13 via the utilized two-step postsynthesis modification procedure. The homogeneous distribution of Sn species in zeolite crystals could be demonstrated by the similar chemical compositions in the surface (measured by XPS analysis) and bulk phase (measured by ICP analysis), which could also be observed from the high angle annular dark field STEM image with elemental mapping (Figure S2 in the Supporting Information).

Catalytic Performance in Epoxide Hydration. The catalytic performance of as-designed zeolite Sn-H-SSZ-13, together with other catalysts for comparison, was investigated in the EO hydration, and the results are shown in Figure 5. No products could be detected without any catalyst, while a very low EO conversion of below 1% was observed with zeolite Na-SSZ-13. In contrast, considerable EO conversion as well as MEG selectivity of above 99% could be obtained with H-SSZ-13, deAl-SSZ-13, Sn-H-SSZ-13, and Sn-Na-SSZ-13 as catalysts (Figure 5a). The perfect MEG selectivity demonstrates the great success of shape-selective catalysis by using catalysts with the CHA structure. The zeolite Sn-H-SSZ-13 exhibits the highest catalytic activity, followed by Sn-Na-SSZ-13 and then deAl-SSZ-13. The catalytic activity of the zeolite Sn-H-SSZ-13 in the EO hydration is distinctly higher than that of the Brønsted acidic zeolite H-ZSM-5 (n_{Si}/n_{Al} = 12) zeolite and Amberlite IR-120 resin as well as homogeneous Brønsted acid H_2SO_4 (1 M) used as reference catalysts but slightly lower than that of the homogeneous Lewis acid Co^{III}(salen). No leaching

of Sn or Al species could be detected by ICP analysis after the reaction, and the possible homogeneous catalysis from leached species could then be excluded. Considering its outstanding MEG selectivity, Sn-H-SSZ-13 is undoubtedly a very attractive solid catalyst for EO hydration.

The effects of the reaction parameters on the catalytic performance of zeolite Sn-H-SSZ-13 were examined in further catalytic studies. As shown in Figure S3a in the Supporting Information, only a weak positive effect of the H_2O/EO ratio on the EO conversion is observed due to the buffering effect from CHA cages as natural nanoreactors. Increasing the reaction temperature promotes the EO conversion over Sn-H-SSZ-13 distinctly but also results in a significant decrease in the MEG selectivity (Figure S3b). This should be due to the fact that high reaction temperatures may induce the further condensation of MEG to DEG and TEG at the outer surface of the zeolite catalyst. Kinetic plots of the EO hydration indicate an increasing EO conversion with reaction time, and specifically, a linear increase of the EO conversion with reaction time could be observed at the initial stage of reaction, e.g. with an EO conversion of below 40%, over deAl-SSZ-13, Sn-H-SSZ-13, and Sn-Na-SSZ-13 (Figure 5b).

During the whole reaction process, the MEG selectivity is kept nearly unchanged (not shown here), confirming that the EO hydration occurs exclusively within the CHA cages of zeolite catalysts. For Sn-H-SSZ-13, an EO conversion of 99.7% with a MEG selectivity of 99.5% could be achieved after reaction at 313 K for 24 h with a H_2O/EO ratio of 2 (a stoichiometric reaction between H_2O and EO would be problematic because of the growing viscosity of the reaction system with the progress of the reaction). The apparent activation energies calculated using the Arrhenius equation are 0.33, 0.38, and 0.41 eV for the catalysis on Sn-H-SSZ-13, Sn-Na-SSZ-13, and deAl-SSZ-13, respectively, while the activation enthalpies calculated using the Eyring equation (Figure 5c) are 0.30, 0.35, and 0.38 eV, respectively. The different apparent activation energies catalyzed by Lewis acidic Sn sites in Sn-H-
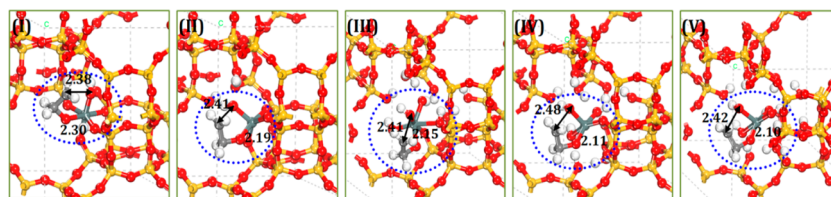
Figure 6. Transition state structures for EO hydration at different active sites of Sn-H-SSZ-13: (I) closed; (II) $Sn(OSi)_3(OH)$; (III) $Sn(OSi)_2(OH)_2$; (IV) $Sn(OSi)(OH)_3$; (V) $Sn(OH)_4$. The bond-forming distances are given in Å.

SSZ-13 and Sn-Na-SSZ-13 should originate from the different local structures of the Lewis acidic sites (vide infra). In addition to the remarkably high activity and selectivity, Sn-H-SSZ-13 also exhibits excellent recyclability in the EO hydration. As shown in Figure 5d, zeolite Sn-H-SSZ-13 could be reused after a simple washing procedure and no activity loss could be observed upon nine cycles.

In summary, it can be stated that Sn-H-SSZ-13 was proved to be a robust solid catalyst for the EO hydration under the desired reaction conditions, i.e. at a low H_2O/EO ratio of 2 and a low reaction temperature of 313 K. The remarkable catalytic performance originating from strong Lewis acidic Sn sites confined in CHA cages and the excellent stability and recyclability demonstrate the great potential of this material as a next-generation catalyst for EO hydration via an energy-saving MEG production process.

Inspired by the great success of zeolite Sn-H-SSZ-13 for EO hydration, we further developed similar catalyst systems, e.g. Sn-H-ZSM-35 and Sn-H-EU-1 (some characterization results are shown in Figure S4 in the Supporting Information), for the hydration of various epoxide substrates to produce the corresponding 1,2-diols. Through a delicately selected framework topology according to the molecule sizes of epoxide substrate and products, the expected high 1,2-diol selectivity could be obtained via diffusion control. For example, the hydration of epoxypropane to 1,2-propanediol and of epichlorohydrin to 3-chloro-1,2-propanediol could be achieved on Sn-H-ZSM-35 with selectivities of 98.1 and 99.5%, respectively (Table 2). That is, water-tolerant Lewis acidic catalysis confined in zeolite cages should be a general strategy for sustainable heterogeneous hydration. Meanwhile, it should be noted that all Sn-zeolites employed here, i.e. Sn-H-SSZ-13, Sn-ZSM-35, Sn-H-EU-1, and Sn-Beta, exhibited considerable activity in the catalytic hydration of EO, while high selectivity to MEG was only achieved on Sn-H-SSZ-13 with diffusion control. These observations confirm the feasibility of shape-selective Lewis acid catalysis confined in the cages of zeolite, as proposed in Figure 1.

Active Sn Sites and Kinetics of the EO Hydration. According to our postsynthesis procedure and characterization results, framework tetrahedral Sn species in both closed and open arrangements might exist in Sn-H-SSZ-13 (Scheme S1 in the Supporting Information). First-principles periodic density functional theory (DFT) calculations were performed to understand the nature of the working active Sn sites and the reaction mechanism of the EO hydration over zeolite Sn-H-SSZ-13. Several theoretical studies have been previously utilized to understand the structure of Sn-beta zeolite and its kinetics in the isomerization of glucose to fructose. It was proposed that the open sites rather than closed sites are more active in Sn-beta.[24a,25] Recently, the presence of active framework Sn species in both open and closed arrangements was confirmed via the combination of dynamic nuclear polarization surface

enhanced NMR spectroscopy and DFT calculations.[26] In our work, the hydration of EO in closed sites was first investigated. As shown in Figure 1, the reaction involves the dissociation of H_2O to form SnOH species and a subsequent ring opening of EO to produce five-membered-ring species. The abstraction of H from the framework and the desorption of EG close the cycle. The dissociation of H_2O was found to be an endothermic step by about 0.7 eV, which undergoes a late transition state. The ring opening of EO is the rate-determining step. The intrinsic overall energy barrier was calculated to be 1.63 eV at the closed site of Sn-H-SSZ-13 (Figures S5 and S6 in the Supporting Information).

The transition state structures for EO hydration at different sites are shown in Figure 6. The kinetics of the EO hydration at four different structures of open sites in zeolite Sn-H-SSZ-13 were further explored. The open sites are built by the hydroxylation to form $Sn(OSi)_m(OH)_n$ ($m + n = 4$) sites to different extents. Silanol nests are then formed accordingly near the active Sn site. These nests are important to stabilize the open active sites through hydrogen bonding. With an increase of the hydroxylation extent, the fully hydroxylated $Sn(OH)_4$ species was finally formed. Because of the presence of hydroxyl groups at the open sites, the EO hydration may involve two different reaction pathways: ring opening of EO as the first step or H_2O coordination to Sn and dissociation as the first step. In this work, the steps of the EO ring opening were studied before or after the coordination/dissociation of H_2O at open $Si(OSi)_3(OH)$, $Si(OSi)_2(OH)_2$, and $Si(OSi)(OH)_3$ sites. As depicted in Figures S7−S9 in the Supporting Information, open sites exhibit higher catalytic activity in the EO hydration and the intrinsic energy barriers for these sites are in the range 0.87−1.34 eV. The reaction pathway involving the EO ring opening as the first step is energetically favored at open $Si(OSi)_3(OH)$ and $Si(OSi)(OH)_3$ sites. In other words, the reaction involving transition states with the six-coordinated structure is not preferred in comparison to that with the five-coordinated structure in some cases. The reaction seems to occur through the step sequence of dissociation of H_2O and ring opening of EO at open $Sn(OSi)_2(OH)_2$ sites (0.92 versus 1.10 eV). When the Sn is fully hydroxylated, it was found that the energy barrier increases dramatically (1.79 eV), and it is even less active than closed sites (1.63 eV) and gaseous $Sn(OH)_4$ (1.39 eV) as a homogeneous catalyst (Figures S5, S10, and S11 in the Supporting Information). The relationship of the energy barrier for the EO hydration with the extent of hydroxylation of the active Sn sites is presented in Figure 7a, where a volcano type shape is observed, while closed sites or fully hydroxylated $Sn(OH)_4$ species exhibit a lower catalytic activity. The catalytic activity reaches a maximum at the open $Sn(OSi)(OH)_3$ site in zeolite Sn-H-SSZ-13. The intrinsic overall energy barrier was calculated to be 0.87 eV. The complete energy profile of EO hydration at $Sn(OSi)(OH)_3$ active sites is shown in Figure 7b. The calculated enthalpy and
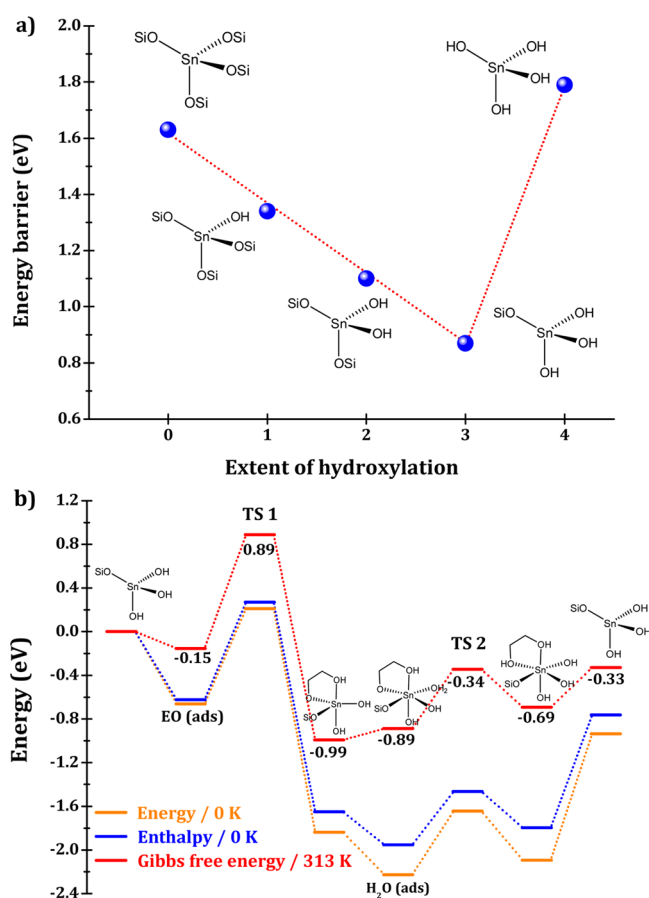
Figure 7. (a) Calculated intrinsic energy barriers in different active sites for EO hydration in Sn-H-SSZ-13, considering EO ring opening as the first step in the reaction pathway. (b) Calculated energy, enthalpy, and Gibbs free energy profiles for EO hydration in the open $Sn(OSi)(OH)_3$ site of Sn-H-SSZ-13.

entropy contributions to the Gibbs free energy barrier at 313 K are 0.23 and 0.65 eV with respect to the gaseous reactants, consistent with the experimental kinetic results (0.30 and 0.53 eV). It should be mentioned that the solvent effect is not considered, as the correction in periodic systems is a great challenge and is beyond the scope of this work.

Advantages of Sn-H-SSZ-13 Catalyzed EO Hydration. With the successful development of a robust Sn-H-SSZ-13 catalyst for EO hydration, new catalytic processes for the MEG production can be expected. Such a process requires much less energy input for heating the reactor and, more important, for the product distillation. It is roughly estimated that the total energy consumption can be reduced from 6 gJ/ton of MEG production for the noncatalytic thermal hydration process to below 3 gJ/ton of MEG production for the new catalytic hydration process. Moreover, only one-fifth of wastewater is generated accompanied by the MEG production in the new catalytic hydration process in comparison to that in the noncatalytic thermal hydration process, which is of great benefit to the environment. Although the long-term stability of the Sn-H-SSZ-13 catalyst is still to be tested and its use may significantly increase the cost of MEG production, the newly established catalytic hydration process indeed shows unparalleled advantages from the perspectives of energy saving and emission reduction.

CONCLUSION

In summary, we have successfully developed a Lewis acid catalyst confined in zeolite cages as a strategy for the sustainable heterogeneous hydration of epoxides. Typically, zeolite Sn-H-SSZ-13 exhibits a remarkable catalytic performance in EO hydration to MEG, and an EO conversion above 99% with a MEG selectivity above 99% can be obtained at approaching stoichiometric H_2O/EO ratios and near-ambient reaction temperatures. Theoretical calculations revealed that the partially hydroxylated Sn species should be the preferred Lewis acid sites for the catalytic hydration of ethylene oxide. The concept presented here can be potentially applied to other catalysts and catalytic processes for a sustainable chemical production.

ASSOCIATED CONTENT

S **Supporting Information**

The Supporting Information is available free of charge on the ACS Publications website at DOI: 10.1021/acscatal.5b02823.

> Scheme for the incorporation of tetrahedrally coordinated Sn(IV) species into SSZ-13 zeolite and additional catalyst characterization, reaction, and calculation data (PDF)

AUTHOR INFORMATION

Corresponding Authors
*E-mail for Z.X.: xzk@sinopec.com.
*E-mail for L.L.: lild@nankai.edu.cn.
Author Contributions
[⊥]These authors contributed equally.

Notes

The authors declare no competing financial interest.

ACKNOWLEDGMENTS

REFERENCES

(1) Wikipedia Home Page. https://en.wikipedia.org/wiki/Ethylene_glycol (accessed Mar 18, 2016).

(2) Shell Global Home Page. http://www.shell.com/business-customers/chemicals/factsheets-speeches-and-articles/factsheets/mono-ethylene-glycol.html (accessed Mar 24, 2016).

(3) (a) Kawabe, K. U.S. Patent 6,080,897, 2000. (b) Kawabe, K.; Nagata, K. U.S. Patent 6,187,972, 2001.

(4) (a) Strickler, G. R.; Landon, V. G.; Lee, G. J. U.S. Patent 6,211,419, 2001. (b) Strickler, G. R.; Lee, G. J.; Rievert, W. J.; Laprairie, D. J.; Timm, E. E. U.S. Patent 6,479,715, 2002.

(5) (a) Li, Y. C.; Yan, S. R.; Yue, B.; Yang, W. M.; Xie, Z. K.; Chen, Q. L.; He, H. Y. *Appl. Catal., A* **2004**, *272*, 305−310. (b) Li, Y. C.; Yan, S. R.; Qian, L. P.; Yang, W. M.; Xie, Z. K.; Chen, Q. L.; Yue, B.; He, H. Y. *J. Catal.* **2006**, *241*, 173−179.

(6) (a) Christen, J. D.; Taylor, H. B. U.S. Patent 4,521,548, 1985. (b) van Hal, J. W.; Ledford, J. S.; Zhang, X. *Catal. Today* **2007**, *123*, 310−315.

(7) Li, B.; Bai, S. Y.; Wang, X. F.; Zhong, M. M.; Yang, Q. H.; Li, C. *Angew. Chem., Int. Ed.* **2012**, *51*, 11517−11521.

(8) Gaikwad, A. V.; Boffa, V.; ten Elshof, J. E.; Rothenberg, G. *Angew. Chem., Int. Ed.* **2008**, *47*, 5407−5410.

(9) (a) Kresse, G.; Furthmuller, J. *Phys. Rev. B: Condens. Matter Mater. Phys.* **1996**, *54*, 11169−11181. (b) Kresse, G.; Joubert, D. *Phys. Rev. B: Condens. Matter Mater. Phys.* **1999**, *59*, 1758−1775. (c) Wellendorff, J.; Lundgaard, K.; Mogelhoj, A.; Petzold, V.; Landis, D.; Norskov, J.; Bligaard, T.; Jacobsen, K. *Phys. Rev. B: Condens. Matter Mater. Phys.* **2012**, *85*, 235149. (d) Henkelman, G.; Jonsson, H. *J. Chem. Phys.* **1999**, *111*, 7010−7022. (e) Wang, C. M.; Brogaard, R. Y.; Weckhuysen, B. M.; Nørskov, J. K.; Studt, F. *J. Phys. Chem. Lett.* **2014**, *5*, 1516−1251. (f) Wang, C. M.; Wang, Y. D.; Du, Y. J.; Yang, G.; Xie, Z. K. *Catal. Sci. Technol.* **2015**, *5*, 4354−4264.

(10) (a) *Shape-Selective Catalysis*; Song, C., Garces, J. M., Sugi, Y., Eds.; American Chemical Society: Washington, DC, 2000; ACS Symposium Series 738. (b) Davis, M. E.; Jones, C. W.; Tsuji, K. *Nature* **1998**, *393*, 52−54. (c) Cheng, Y.-T.; Wang, Z.; Gilbert, C. J.; Fan, W.; Huber, G. W. *Angew. Chem., Int. Ed.* **2012**, *51*, 11097−11110. (d) Jacobs, P. A.; Dusselier, M.; Sels, B. F. *Angew. Chem., Int. Ed.* **2014**, *53*, 8621−8626. (e) Dusselier, M.; Van Wouwe, P.; Dewaele, A.; Jacobs, P. A.; Sels, B. F. *Science* **2015**, *349*, 78−80.

(11) First, E. L.; Gounaris, C. E.; Wei, J.; Floudas, C. A. *Phys. Chem. Chem. Phys.* **2011**, *13*, 17339−17358.

(12) Zones, S. I. U.S. Patent 4,544,538, 1985.

(13) van Hal, J.; Ramprasad, D. U.S. Patent 6,916,963, 2005.

(14) (a) Corma, A.; Nemeth, L. T.; Renz, M.; Valencia, S. *Nature* **2001**, *412*, 423−425. (b) Corma, A.; Domine, M. E.; Nemeth, L.; Valencia, S. *J. Am. Chem. Soc.* **2002**, *124*, 3194−3195. (c) Osmundsen, C. M.; Holm, M. S.; Dahl, S.; Taarning, E. *Proc. R. Soc. London, Ser. A* **2012**, *468*, 2000−2016. (d) Hammond, C.; Conrad, S.; Hermans, I. *Angew. Chem., Int. Ed.* **2012**, *51*, 11736−11739. (e) Roy, S.; Bakhmutsky, K.; Mahmoud, E.; Lobo, R. F.; Gorte, R. J. *ACS Catal.* **2013**, *3*, 573−580. (f) Ren, L.; Guo, Q.; Kumar, P.; Orazov, M.; Xu, D.; Alhassan, S. M.; Mkhoyan, K. A.; Davis, M. E.; Tsapatsis, M. *Angew. Chem., Int. Ed.* **2015**, *54*, 10848−10851.

(15) (a) Román-Leshkov, Y.; Davis, M. E. *ACS Catal.* **2011**, *1*, 1566−1580. (b) Moliner, M.; Román-Leshkov, Y.; Davis, M. E. *Proc. Natl. Acad. Sci. U. S. A.* **2010**, *107*, 6164−6168. (c) Holm, M. S.; Saravanamurugan, S.; Taarning, E. *Science* **2010**, *328*, 602−605. (d) Gunther, W. R.; Wang, Y.; Ji, Y.; Michaelis, V. K.; Hunt, S. T.; Griffin, R. G.; Román-Leshkov, Y. *Nat. Commun.* **2012**, *3*, 1109. (e) Dusselier, M.; Van Wouwe, P.; Dewaele, A.; Makshina, E.; Sels, B. F. *Energy Environ. Sci.* **2013**, *6*, 1415−1442. (f) Cho, H. J.; Dornath, P.; Fan, W. *ACS Catal.* **2014**, *4*, 2029−2037.

(16) (a) Tang, B.; Dai, W.; Wu, G.; Guan, N.; Li, L.; Hunger, M. *ACS Catal.* **2014**, *4*, 2801−2810. (b) Tang, B.; Dai, W.; Sun, X.; Guan, N.; Li, L.; Hunger, M. *Green Chem.* **2014**, *16*, 2281−2291.

(17) (a) Price, S. J. W.; Trotman-Dickenson, A. F. *Trans. Faraday Soc.* **1958**, *54*, 1630−1636. (b) Nash, G. A.; Skinner, H. A.; Stack, W. F. *Trans. Faraday Soc.* **1965**, *61*, 640−648. (c) van Mol, A. M. B.; de Croon, M. H. J. M.; Spee, C. I. M. A.; Schouten, J. C. *J. Phys. IV* **1999**, *09*, Pr8-165−Pr8-172.

(18) Fritz, P. O.; Lunsford, J. H. *J. Catal.* **1989**, *118*, 85−98.

(19) Dai, W.; Sun, X.; Tang, B.; Wu, G.; Guan, N.; Li, L.; Hunger, M. *J. Catal.* **2014**, *314*, 10−20.

(20) (a) Prasad, S.; Petrov, M. *Solid State Nucl. Magn. Reson.* **2013**, *54*, 26−31. (b) Sykes, D.; Kubicki, J. D.; Farrar, T. C. *J. Phys. Chem. A* **1997**, *101*, 2715−2722.

(21) Hunger, M. *Catal. Rev.: Sci. Eng.* **1997**, *39*, 345−393.

(22) (a) Li, S. H.; Zheng, A. M.; Su, Y. C.; Zhang, H. L.; Chen, L.; Yang, J.; Ye, C. H.; Deng, F. *J. Am. Chem. Soc.* **2007**, *129*, 11161−11171. (b) Barich, D. H.; Nicholas, J. B.; Xu, T.; Haw, J. F. *J. Am. Chem. Soc.* **1998**, *120*, 12342−12350. (c) Su, X.; Xu, S. T.; Tian, P.; Li, J. Z.; Zheng, A. M.; Wang, Q.; Yang, M.; Wei, Y. X.; Deng, F.; Liu, Z. M. *J. Phys. Chem. C* **2015**, *119*, 2589−2596. (d) Dai, W. L.; Wang, X.; Wu, G. J.; Li, L. D.; Guan, N. J.; Hunger, M. *ChemCatChem* **2012**, *4*, 1428−1435.

(23) Pachamuthu, M. P.; Shanthi, K.; Luque, R.; Ramanathan, A. *Green Chem.* **2013**, *15*, 2158−2166.

(24) (a) Bermejo-Deval, R.; Assary, R. S.; Nikolla, E.; Moliner, M.; Román-Leshkov, Y.; Hwang, S.-J.; Palsdottir, A.; Silverman, D.; Lobo, R. F.; Curtiss, L. A.; Davis, M. E. *Proc. Natl. Acad. Sci. U. S. A.* **2012**, *109*, 9727−9732. (b) Gunther, W. R.; Michaelis, V. K.; Caporini, M. A.; Griffin, R. G.; Román-Leshkov, Y. *J. Am. Chem. Soc.* **2014**, *136*, 6219−6222.

(25) (a) Boronat, M.; Concepcion, P.; Corma, A.; Renz, M.; Valencia, S. *J. Catal.* **2005**, *234*, 111−118. (b) Yang, G.; Pidko, E. A.; Hensen, E. J. *ChemSusChem* **2013**, *6*, 1688−1696. (c) Dijkmans, J.; Dusselier, M.; Janssens, W.; Trekels, M.; Vantomme, A.; Breynaert, E.; Kirschhock, C.; Sels, B. F. *ACS Catal.* **2016**, *6*, 31−46.

(26) Wolf, P.; Valla, M.; Rossini, A. J.; Comas-Vives, A.; Núñez-Zarur, F.; Malaman, B.; Lesage, A.; Lyndon Emsley, L.; Copéret, C.; Hermans, I. *Angew. Chem.* **2014**, *126*, 10343−10347.